

Disentangling types of lattice disorder impacting superconductivity in Sr_2RuO_4 by quantitative local probes

Cite as: APL Mater. **10**, 041114 (2022); <https://doi.org/10.1063/5.0085279>

Submitted: 14 January 2022 • Accepted: 23 March 2022 • Published Online: 29 April 2022

 Berit H. Goodge, Hari P. Nair, David J. Baek, et al.

COLLECTIONS

 This paper was selected as an Editor's Pick



View Online



Export Citation



CrossMark

ARTICLES YOU MAY BE INTERESTED IN

Chinese Abstracts

Chinese Journal of Chemical Physics **35**, i (2022); <https://doi.org/10.1063/1674-0068/35/01/cabs>

Simple apparatus for demonstrating factors that influence lift and drag

American Journal of Physics **90**, 359 (2022); <https://doi.org/10.1119/10.0009681>

Cooling rate and dendrite spacing control in direct metal deposition printed Cu-Fe alloys

Journal of Laser Applications **34**, 022013 (2022); <https://doi.org/10.2351/7.0000464>

APL Materials

SPECIAL TOPIC:
Materials Challenges for Supercapacitors

Submit Today!



Disentangling types of lattice disorder impacting superconductivity in Sr_2RuO_4 by quantitative local probes

Cite as: APL Mater. 10, 041114 (2022); doi: 10.1063/5.0085279

Submitted: 14 January 2022 • Accepted: 23 March 2022 •

Published Online: 29 April 2022














View Online



Export Citation



CrossMark

Berit H. Goodge,^{1,a)}  Hari P. Nair,²  David J. Baek,³  Nathaniel J. Schreiber,²  Ludi Miao,⁴  Jacob P. Ruf,^{4,b)} 
Emily N. Waite,^{1,c)}  Philip M. Carubia,²  Kyle M. Shen,^{4,5}  Darrell G. Schlom,^{2,5,6} 
and Lena F. Kourkoutis^{1,5,a)} 

AFFILIATIONS

¹School of Applied and Engineering Physics, Cornell University, Ithaca, New York 14853, USA

²Department of Materials Science and Engineering, Cornell University, Ithaca, New York 14853, USA

³School of Electrical and Computer Engineering, Cornell University, Ithaca, New York 14853, USA

⁴Department of Physics, Cornell University, Ithaca, New York 14853, USA

⁵Kavli Institute at Cornell for Nanoscale Science, Cornell University, Ithaca, New York 14853, USA

⁶Leibniz-Institut für Kristallzüchtung, Max-Born-Str. 2, 12489 Berlin, Germany

^{a)}Authors to whom correspondence should be addressed: bhg37@cornell.edu and lena.f.kourkoutis@cornell.edu

^{b)}Current address: Max Planck Institute for Chemical Physics of Solids, 01187 Dresden, Germany.

^{c)}Current address: Department of Physics and Materials Research Laboratory, University of Illinois, Urbana, IL 61801, USA.

ABSTRACT

The unconventional superconductivity in Sr_2RuO_4 is infamously susceptible to suppression by small levels of disorder such that it has been most commonly studied in extremely high-purity bulk crystals. Here, we harness local structural and spectroscopic scanning transmission electron microscopy measurements in epitaxial thin films of Sr_2RuO_4 to disentangle the impact of different types of crystalline disorder on superconductivity. We find that cation off-stoichiometry during growth gives rise to two distinct types of disorder: mixed-phase structural inclusions that accommodate excess ruthenium and ruthenium vacancies when the growth is ruthenium-deficient. Several superconducting films host mixed-phase intergrowths, suggesting this microstructural disorder has relatively little impact on superconductivity. In a non-superconducting film, on the other hand, we measure a high density of ruthenium-vacancies ($\sim 14\%$) with no significant reduction in the crystallinity of the film. The results suggest that ruthenium vacancy disorder, which is hidden to many structural probes, plays an important role in suppressing superconductivity. We discuss the broader implications of our findings to guide the future synthesis of this and other layered systems.

© 2022 Author(s). All article content, except where otherwise noted, is licensed under a Creative Commons Attribution (CC BY) license (<http://creativecommons.org/licenses/by/4.0/>). <https://doi.org/10.1063/5.0085279>

I. INTRODUCTION

Complex oxides are a rich class of materials hosting a wide range of exotic and functional properties, including superconductivity,^{1–3} multiferroicity,^{4,5} magnetism,⁷ and other strongly correlated behaviors.⁸ The root of these phenomena is the subtle interplay between lattice, charge, orbital, and spin degrees of freedom, finely tunable through precise structural and

chemical control. Yet despite their myriad applications for both fundamental science and technological advances, ultimately the use of these correlated materials is limited by the robustness of their properties to the kinds of disorder which are a practical reality in all samples. Realizing the full potential of these systems therefore relies on understanding the impact different types of disorder have

on functional properties and on finding strategic routes to avoid the most detrimental.

Particularly in systems where disorder and other forms of heterogeneity play a key role in the materials properties, the ability to identify and isolate experimental signals from distinct regions is essential. Spatially resolved measurements by high-angle annular dark-field (HAADF) imaging and electron energy loss spectroscopy (EELS) in the scanning transmission electron microscope (STEM) offer the ability to directly probe local lattice and electronic structure, making them uniquely poised for quantitative characterization of crystalline materials down to the atomic scale.^{9–14}

In this report, we employ high-resolution STEM-EELS across a series of Sr₂RuO₄ thin films grown by molecular-beam epitaxy (MBE) to disentangle the impacts on superconductivity of distinct types of structural disorder. Despite its relatively simple Fermi surface and normal state description, a microscopic understanding of the superconducting state of Sr₂RuO₄ has remained out of reach after more than two decades of experimental and theoretical efforts.¹⁵ One complicating factor has been a strict requirement of extremely low-disorder samples, which for many years limited the accessible experimental geometries to mostly bulk-synthesized crystals. Compared to the relatively robust superconductivity in other oxide families—particularly cuprates¹⁶—superconductivity in Sr₂RuO₄ is extremely sensitive to crystalline disorder.^{17,18} Due in part to this sensitivity, the successful synthesis of superconducting samples in the thin film geometry is particularly challenging.^{19–22} In recent years, efforts to grow superconducting thin films of Sr₂RuO₄ by MBE have produced high-quality samples with superconducting transition temperatures on par or higher than unstrained bulk crystals.²² The properties of these films, however, are extremely sensitive to the specific growth conditions, and small deviations outside of the thermodynamic growth window produce films that look structurally similar, yet exhibit persistent metallic transport signatures down to 0.4 K (the limit of our measurements) without undergoing a superconducting transition. XRD and other bulk probes do not show an obvious reduction in the crystalline quality of non-superconducting samples, motivating a detailed investigation of possible nano-scale effects in these films. Using local structural and spectroscopic measurements in several Sr₂RuO₄ thin films, we reveal two distinct forms of structural disorder with nonequivalent impact on superconductivity. In particular, atomic-resolution HAADF-STEM imaging reveals that some superconducting films of Sr₂RuO₄ show much higher occurrence of Ruddlesden–Popper²³ Sr_{*n*+1}Ru_{*n*}O_{3*n*+1} with *n* > 1 intergrowths²⁴ than non-superconducting films. Even at high densities, these intergrowths have relatively little effect on the macroscopic superconductivity of a given film. Non-superconducting films, on the other hand, can show surprisingly near-perfect adherence to the Sr₂RuO₄ nominal crystalline structure, as has also been reported previously.²⁵ Local spectroscopic analysis reveals a significant density of ruthenium vacancies in these samples (~14%), which are thus determined to be responsible for suppressing superconductivity in otherwise apparently well-ordered films.

II. METHODS

A. Thin film growth

The Sr₂RuO₄ thin films characterized here were grown on (110) NdGaO₃ substrates from CrysTec GmbH in a Veeco Gen 10 MBE

system within an adsorption-controlled growth window as previously described.^{22,26} Strontium (99.99% pure) was evaporated from a low temperature effusion cell while an electron beam evaporator was used for ruthenium (99.99% pure), with distilled ozone (~80% O₃ + 20% O₂) used as the oxidant. The strontium and ruthenium fluxes and estimated ozone pressures for each film are reported in Table 1 of the [supplementary material](#). At the end of each growth, both the strontium and ruthenium shutters were closed simultaneously and the sample was rapidly cooled to below 250 °C under the same ozone pressure used during growth. A 30 nm SrRuO₃ thick film grown on (110) NdGaO₃ described elsewhere²⁷ was also used as a standard reference sample for scanning electron microscope energy-dispersive x-ray spectroscopy measurements.

B. Macroscopic structure and transport measurements

A Rigaku SmartLab high-resolution diffractometer with Cu-Kα1 radiation ($\lambda = 1.5406 \text{ \AA}$) was used to carry out x-ray diffraction (XRD) measurements along the specular crystal truncation rod (CTR). The incident side optics for the XRD θ - 2θ measurement used a Ge 220 double-crystal monochromator along with a Ge 220 two-bounce analyzer on the detector side to improve the resolution rocking curve measurements of the Sr₂RuO₄ 006 reflection. Incident and receiving side optics slits were set to 1 mm. The full width at half maximum (FWHM) of the Sr₂RuO₄ peak for each film is ~20 arcsec, indicating high structural quality comparable to the NdGaO₃ substrates with peak FWHM ~15 arcsec (see Fig. S1 in the [supplementary material](#)).

Electrical transport measurements as a function of temperature from 300 K down to 0.4 K were conducted in a Quantum Design Physical Property Measurement System (PPMS) equipped with a ³He insert. Aluminum wires from gold pads on the PPMS sample holder were wire bonded directly to the surface of the films in a four-point linear geometry, spaced ~2 mm apart along the longer dimension of the sample. The in-plane residual resistivity ratio (RRR) [$\rho_{ab}(300\text{K})/\rho_{ab}(4\text{K})$] for each film is given in [Table I](#). We note that the films were not patterned prior to resistance measurements, so the electrical current was not constrained to flow along a particular in-plane direction of the films. In such a contact geometry, the measured resistance *R* is proportional to the geometric mean of the diagonal components of the in-plane resistivity tensor, $\rho \equiv \sqrt{\rho_{xx} * \rho_{yy}}$, via conversion factors determined by the total film thicknesses and lateral separations between contacts.^{28,29} The resistively measured *T_c*s are the temperature scales below which percolative superconducting pathways first develop between the electrical contacts ([Table I](#)).

C. SEM-EDX

Energy-dispersive x-ray spectroscopy (EDX) in a scanning electron microscope (SEM) was performed on a Zeiss Gemini 500 operating at 8 kV equipped with an Oxford Ultim Max 170 x-ray detector. Atomic percent concentrations of strontium and ruthenium were calculated using the L series lines based on factory calibrations of SrF₂ and Ru (V), respectively. Some thin-film samples contain visible mesoscopic precipitates of ruthenium metal similar to those documented in other Sr₂RuO₄ systems;^{30,31} in these cases, measurements were localized in “clean” regions, as judged

TABLE I. Relative Ru/Sr stoichiometries measured by SEM-EDX for the Sr₂RuO₄ films in Fig. 1 and their superconducting transition temperatures T_c . Measurement of a SrRuO₃ film is also provided for reference.

Nominal structure	Substrate	Thickness (nm)	RRR	T_c	EDX Ru/Sr ratio
Sr ₂ RuO ₄	(110) NdGaO ₃	36	15.7	–	0.51
Sr ₂ RuO ₄	(110) NdGaO ₃	71	45.0	1.4 K	0.59
Sr ₂ RuO ₄	(110) NdGaO ₃	55	69.1	1.8 K	0.53
SrRuO ₃	(110) NdGaO ₃	30	21.4	–	1.06

by surface contrast in the SEM to the best of our ability (see Fig. S2 in the [supplementary material](#)), to exclude contributions from these impurities. Additional characterization and discussion of the precipitates observed in our films is provided in Fig. S3 in the [supplementary material](#).

D. STEM imaging

Cross-sectional STEM specimens were prepared using the standard focused ion beam (FIB) lift-out process on an FEI Strata 400 FIB equipped with an Omniprobe AutoProbe 200 nanomanipulator. All resulting lamellae were thinned to final thicknesses of 15–60 nm. The results presented here are from specimens prepared to similar projection thicknesses, which is an important consideration for STEM-EELS measurements. These measurements were carried out on the same day to ensure that all other aspects of the experimental setup (e.g., microscope and spectrometer alignments) were as similar as possible. High-angle annular dark-field scanning transmission electron microscopy (HAADF-STEM) images were acquired on an aberration-corrected 300 keV FEI Titan Themis with a probe convergence semi-angle of 30 mrad and inner and outer collection angles of 68 and 340 mrad, respectively.

E. Layer-resolved EELS

Spatially resolved electron energy loss spectroscopy (EELS) was performed on the same Titan Themis system, equipped with a 965 GIF Quantum ER and a Gatan K2 Summit operated in electron counting mode with a spectral dispersion of 0.25 eV/ch. Using a sub-Å STEM probe, the scan was confined to specific layers of interest over areas on the order of 50–100 nm² in order to probe each structural phase separately. Given the relative sensitivity of ruthenate compounds to the electron beam, low beam currents (~20 pA) and acquisition times of 500 s were used for all spectra shown here. The enhanced sensitivity and point spread function of the EELS direct electron detector are ideal for optimizing measurements on sensitive samples, providing an effective energy resolution of ~1 eV over a full spectral range of 927 eV for simultaneous acquisition of the Sr-M_{2,3}, Ru-M_{4,5}, and O-K edges.³² All EEL spectra were acquired as summed series and analyzed to ensure that no dose-dependent effects were introduced during the measurement (i.e., no observable signs of damage or spectral modification from the initial to the final measurement). Measurements of the nominally $n = 1$ phases in both the superconducting $T_c = 1.4$ K and non-superconducting films were acquired in three different regions of the STEM lamellae. Stoichiometric estimates for the non-superconducting film are based upon the average of these individual measurements, which are also shown. All spectra presented here are

unfiltered, with the exception of the O-K edge pre-peak reproduced in Fig. 4(b), of which an identical but unfiltered plot is provided in Fig. S4 in the [supplementary material](#).

The inelastic background of each spectrum is removed by fitting and subtracting either a power law $c\Delta E^{-r}$ (for the O-K edge) or a decaying exponential function $ce^{-r\Delta E}$ (for Sr-M_{2,3}/Ru-M_{4,5} edges), where ΔE is the energy loss in eV and c and r are constants determined by least squares minimization. Power law fits are commonly used for EELS analysis of core-loss edges like the O-K edge,³³ though other models can also be used when they are found to more accurately describe the spectroscopic background. In the lower energy-loss region of the spectrum where the Sr-M_{2,3} and Ru-M_{4,5} edges occur, decaying exponential fits were empirically determined to provide more appropriate and robust models. Spectral Ru/Sr ratios were calculated as the quotient of each spectrum integrated between 313–350 eV (Ru) and 269–280 eV (Sr).

III. RESULTS

Structural characterization by XRD and electrical characterization by transport measurements for three Sr₂RuO₄ films studied in detail are presented in Fig. 1. X-ray diffraction θ - 2θ scans for the films are shown in Fig. 1(a), illustrating similar and apparently high crystalline quality for all three samples. The electrical transport in Fig. 1(b), however, indicates that not all films exhibit superconducting transitions. One of the samples remains metallic but non-superconducting down to the lowest measured temperature (~0.4 K), while the other two undergo superconducting transitions at 1.4 and 1.8 K, respectively, defined by the point where the resistivity has dropped by 50% through the transition. To distinguish between these films in the following discussions, we hereafter refer to the samples by the temperature of their superconducting transition: non-superconducting (nSC), $T_c = 1.4$ K, and $T_c = 1.8$ K. The higher-than-bulk T_c of the 1.8 K sample is discussed elsewhere,²² demonstrating the power of epitaxially strained thin film growth to raise T_c above that of single crystals.

Despite their apparently similar macroscopic crystalline quality as measured by XRD, the atomic-resolution HAADF-STEM images shown in Fig. 2 provide more detailed information about the microstructural character of each film. All three films show coherent epitaxial interfaces with the (110) NdGaO₃ substrates and no signs of chemical diffusion across the film-substrate interface within the limit of elemental mapping measurements by EELS. The precise structure of the interface varies slightly between regions and films in the exact arrangement of SrO and RuO₂ planes, but the intended Sr₂RuO₄ structure is usually achieved within ~2 nm of the interface.³⁴ The non-superconducting film shown in Fig. 2(a)

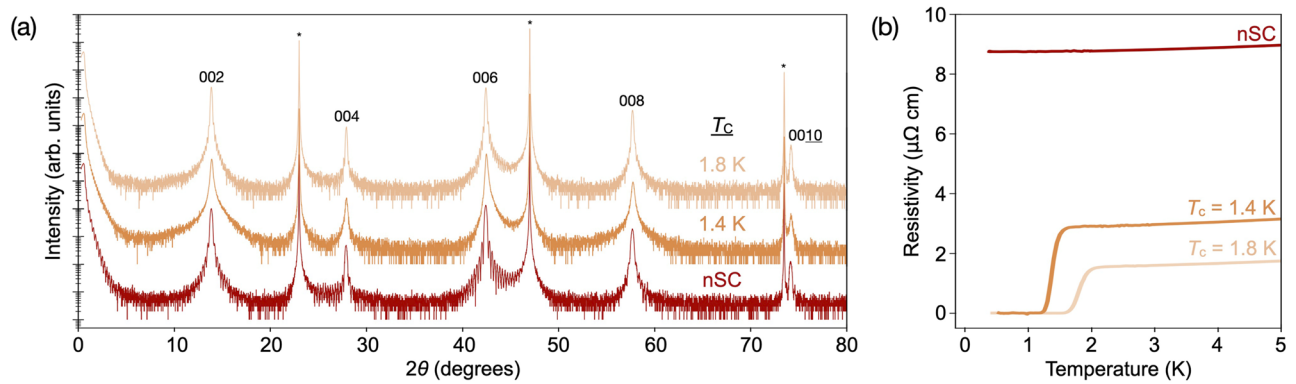


FIG. 1. (a) X-ray diffraction θ – 2θ scans with film peaks indexed (substrate peaks marked by asterisks) and (b) transport measurements of the same three Sr_2RuO_4 thin films grown by MBE on (110) NdGaO_3 . One film (red) is non-superconducting (nSC) down to 0.4 K. Two films (light and dark orange) show superconducting transitions at 1.4 and 1.8 K, respectively. XRD and transport measurements for the $T_c = 1.8$ K film are reproduced from Ref. 22.

exhibits a near-perfect adherence to the Sr_2RuO_4 structure. Some extended defects are observed throughout the film (see Fig. S5 in the [supplementary material](#)). The characteristic spacing between such defects, however, is lower than the superconducting coherence length of Sr_2RuO_4 (~ 75 nm)¹⁵ and are, therefore, not expected to disrupt superconductivity as in previously reported samples with higher defect density.^{34,35} We have also observed similar defects with comparable spacing in other superconducting Sr_2RuO_4 thin films with relatively high T_c .³⁶ The $T_c = 1.8$ K film in Fig. 2(c) shows similar structural quality to the non-superconducting film, with limited interruption to the Sr_2RuO_4 structure occurring as local step-edges such as those seen near the center of the image.

In contrast to these endmembers, the $T_c = 1.4$ K superconducting film in Fig. 2(b) also shows significant structural variation in

the form of $\text{Sr}_{n+1}\text{Ru}_n\text{O}_{3n+1}$ inclusions with $n > 1$. Fig. S6 in the [supplementary material](#) shows several representative images comparing the mixed-phase microstructure in the two superconducting films. These intergrowths constitute the first form of obvious structural disorder that we investigate in detail.

A. Ruddlesden–Popper phase intergrowths

Several other superconducting films of varying thicknesses with T_c s in the range of 0.7–1.6 K show similar higher- n layer inclusions and $n = 2$ phase intergrowths have also been reported in superconducting crystals synthesized in bulk^{24,37} and by other thin-film techniques.³⁴ A histogram comparing statistical occurrences of different local n -phases in each of the three films studied here as well as several others included in our broader investigation is provided in

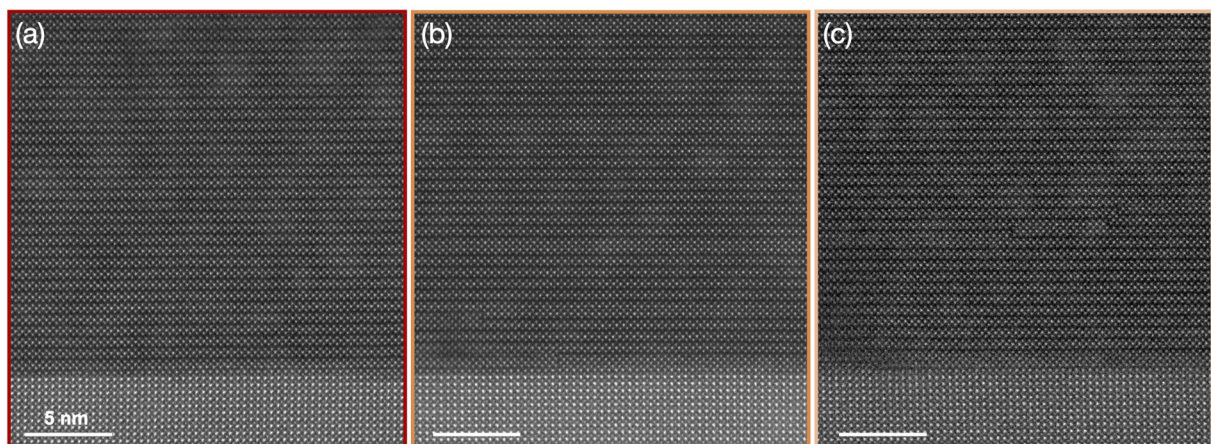


FIG. 2. Atomic-resolution HAADF-STEM cross-sectional images of the same three Sr_2RuO_4 films shown in Fig. 1: (a) non-superconducting (nSC) film, (b) superconducting film with $T_c = 1.4$ K, and (c) superconducting film with $T_c = 1.8$ K. Additional details for each film are provided in Table I. All three films show a coherent epitaxial interface with the (110) NdGaO_3 substrate. The $T_c = 1.4$ K film in particular shows a notable density of $n > 1$ $\text{Sr}_{n+1}\text{Ru}_n\text{O}_{3n+1}$ syntactic intergrowths.

Fig. S7 in the [supplementary material](#). We start by neglecting point defects and their impact on film composition. Within this assumption, across the broader class of $A_{n+1}B_nO_{3n+1}$ Ruddlesden–Popper compounds, a material’s structural phase is directly tied to the relative cation stoichiometry through the relation,

$$\frac{[B]}{[A]} = \frac{n}{n+1}, \quad (1)$$

where $[A]$ and $[B]$ are the elemental concentrations of each species. Deviations from a particular Ruddlesden–Popper motif can therefore be considered a structural accommodation of global sample off-stoichiometry.^{6,38} In principle, the elemental ratio of $[B]/[A]$ can thus be used to distinguish between different $A_{n+1}B_nO_{3n+1}$ phases: as n increases, so does the $[B]/[A]$ ratio $n/(n+1)$ until it reaches unity for the $n = \infty$ perovskite phase ABO_3 .

We correspondingly investigated the elemental stoichiometric ratios of the three films shown in [Fig. 1](#) as well as an MBE-grown $SrRuO_3$ reference film via SEM-EDX, presented in [Table I](#). Precise and accurate quantitative measurements of thin-film stoichiometry by SEM-EDX can be complicated by a number of factors including fluorescence effects and sample roughness, but it can be a useful tool for preliminary comparison between samples with similar geometries. All of the films measured here by SEM-EDX are of thicknesses (~ 30 – 70 nm) which are similarly small compared to the interaction volume for 8 kV primary electrons. Measurements of the reference $SrRuO_3$ film give a sense of the error inherent to this kind of measurement,³⁹ as the calculated Ru/Sr ratio of 1.06 suggests a Ruddlesden–Popper phase $n > \infty$, which is nonphysical. Such apparent excess could also be ascribed to second-phase precipitates of RuO_2 or ruthenium metal or strontium vacancies similar to those described in other off-stoichiometric Ruddlesden–Popper systems.^{38,40} As described in [Sec. II](#), however, care was taken to localize the SEM-EDX measurements away from obvious inclusions or precipitates within the films ([Figs. S1 and S3](#) in the [supplementary material](#)), and the RRR value of 21.4 of this film suggests the density of strontium vacancies (and subsequent disorder) is low ([Fig. S8](#) in the [supplementary material](#)).^{27,41,42} Still, despite these quantitative challenges, the results for the two superconducting Sr_2RuO_4 films are qualitatively consistent with the relative density of microstructural inclusions revealed by HAADF-STEM: the $T_c = 1.4$ K film shows both more structural intergrowths and a higher Ru/Sr elemental ratio than the $T_c = 1.8$ K film.

Having determined that these defects are a reflection of elemental off-stoichiometry in the films, we consider their impact on superconductivity. The statistical occurrence and distribution of high- n layers was analyzed across several superconducting thin films ([Fig. S7](#) in the [supplementary material](#)), but no trend was found connecting these structural variations with the occurrence or onset temperature of superconductivity. Based on this analysis, we conclude that the high- n inclusions have little impact on the bulk superconductivity of a given thin film, but that they can instead be considered mostly inert within the context of superconductivity when a supercurrent can find a percolation path around them. This conclusion along with the apparent microstructural quality of the non-superconducting film shown in [Fig. 2\(a\)](#) suggests that conventional descriptions of sample quality such as phase purity are not

always sufficient metrics to predict exotic behavior such as superconductivity in Sr_2RuO_4 . Instead, the relative elemental ratios in [Table I](#) hint at a second form of disorder in these systems to which we now turn our attention.

B. Ruthenium vacancies

The non-superconducting film appears by both HAADF-STEM imaging and SEM-EDX measurements as the “most perfect” Sr_2RuO_4 of the three films studied here, forcing us to revisit the above assumption that neglected possible point defects. The relation in [Eq. \(1\)](#) and its application for assessing mixed Ruddlesden–Popper n phases become limited when the ratios approach $1/2$ or smaller. Just as $n > \infty$ Ruddlesden–Popper phases are nonphysical, so also are $n < 1$. Although the absolute elemental Ru/Sr ratio measured for the non-superconducting film is slightly more than $1/2$, the value is relatively less than that of the $T_c = 1.8$ K film. Even accounting for the observed non-zero occurrence of higher- n regions in the $T_c = 1.8$ K film (which will drive up the average measured Ru/Sr ratio), this comparison suggests subtle stoichiometric differences between the two films, similar to those previously studied in more extreme cases.²⁵

While the qualitative trend of the SEM-EDX measurements is instructive, the microstructural insights from HAADF-STEM imaging prove the existence of mixed structural phases within some films, which have direct impact on this kind of depth-averaged elemental quantification. Having already determined that these inclusions do not contribute to the film’s transport, we instead seek to quantify the local stoichiometry of only the $n = 1$ layers which are relevant for superconductivity. The SEM-EDX results also underscore the difficulty of exact stoichiometric quantification through any spectroscopic technique, the accuracy and precision of which rely on careful calibration. To address both of these challenges and to quantify ruthenium vacancies that may be present in the non-superconducting film, we next leverage highly localized EELS measurements to create an internal stoichiometric calibration based on the high- n intergrowths in the $T_c = 1.4$ K film.

One common way to probe stoichiometry via EELS is based on identifying the electronic valence of a particular element and then inferring its relative concentration from a balanced chemical formula.^{43,44} Successful application of this technique is limited to elements with ionization edges for which the near-edge fine structure can be used as spectroscopic signature of valence (e.g., $L_{2,3}$ edges to probe $2p \rightarrow 3d$ transitions in the period four transition metals, or $M_{4,5}$ edges to probe $3d \rightarrow 4f$ transitions in the period five transition metals). In some cases, this strategy may be rendered ineffective by hybridization effects that complicate the interpretation of the EELS fine structure⁴⁵ or small ionization cross sections that result in weak signals and prevent the collection of very high signal-to-noise ratio spectra, especially if spatial resolution is to be retained. Furthermore, the valence-based approach is most effective for binary compounds in which knowing the valence of one element will necessarily dictate the concentrations required to create a neutral compound. In the complex oxides, however, there may exist multiple stoichiometric configurations consistent with the measured valence for a given cation. Consider, for example, off-stoichiometric deviations from a balanced compound $A^{2+}B^{4+}(O^{2-})_3$. In this case, a decrease in the A-site cation valence ($A^{(2-\delta)+}$) could reflect either deficiency in O

$[(O^{2-})_{(3-\delta/2)}]$, an excess of the B -site cation $[(B^{4+})_{(1+\delta/4)}]$, or some globally averaged combination of the two. These analytic complications combined with the relative weakness of the desired edges in Sr_2RuO_4 (Sr- $M_{2,3}$ and Ru- $M_{4,5}$) make this method unsuitable for stoichiometric measurements of our thin films.

Instead, we employ a method conceptually similar to standard EDX analysis. In principle, EELS measurements can also be used to extract relative concentrations of two elements A and B using the relation,

$$\frac{[B]}{[A]} = \frac{I_B}{I_A} \times \frac{\sigma_B}{\sigma_A}, \quad (2)$$

where $[A]$ and $[B]$ are the atomic volume density, I is the core-loss edge spectral intensity, and σ is the partial scattering cross section for each species.⁴⁶ The scattering cross sections $\sigma_{A,B}$ must be either calculated theoretically or calibrated experimentally from a sample with a precisely-known $[B]/[A]$ ratio. In practice, the quantitative comparison between separate EELS measurements can be

greatly complicated by other variables in the experiment, including STEM probe conditions, spectrometer tuning and alignments, and sample-to-sample thickness variations, which affect multiple scattering and spectral backgrounds. Here, we avoid several of these complicating factors by harnessing the local higher- n phase $Sr_{n+1}Ru_nO_{3n+1}$ inclusions in a single STEM lamella of the $T_c = 1.4$ K superconducting film. The $n > 1$ layers provide a series of built-in stoichiometric references for calibrating local spectroscopic measurements with systematically varying B/A (Ru/Sr) across the Ruddlesden–Popper series. Constructing the calibration with multiple measurements from within the same lamella is inherently independent of major sample-to-sample variations such as lamella thickness. When comparing between two samples (i.e., the $T_c = 1.4$ K and non-superconducting films), performing all EELS measurements on the same day helps ensure consistency across the instrumental factors, including the STEM probe and spectrometer conditions. The data reported here were collected from regions with comparable projection thickness (~ 20 nm) to minimize the effects of multiple scattering.

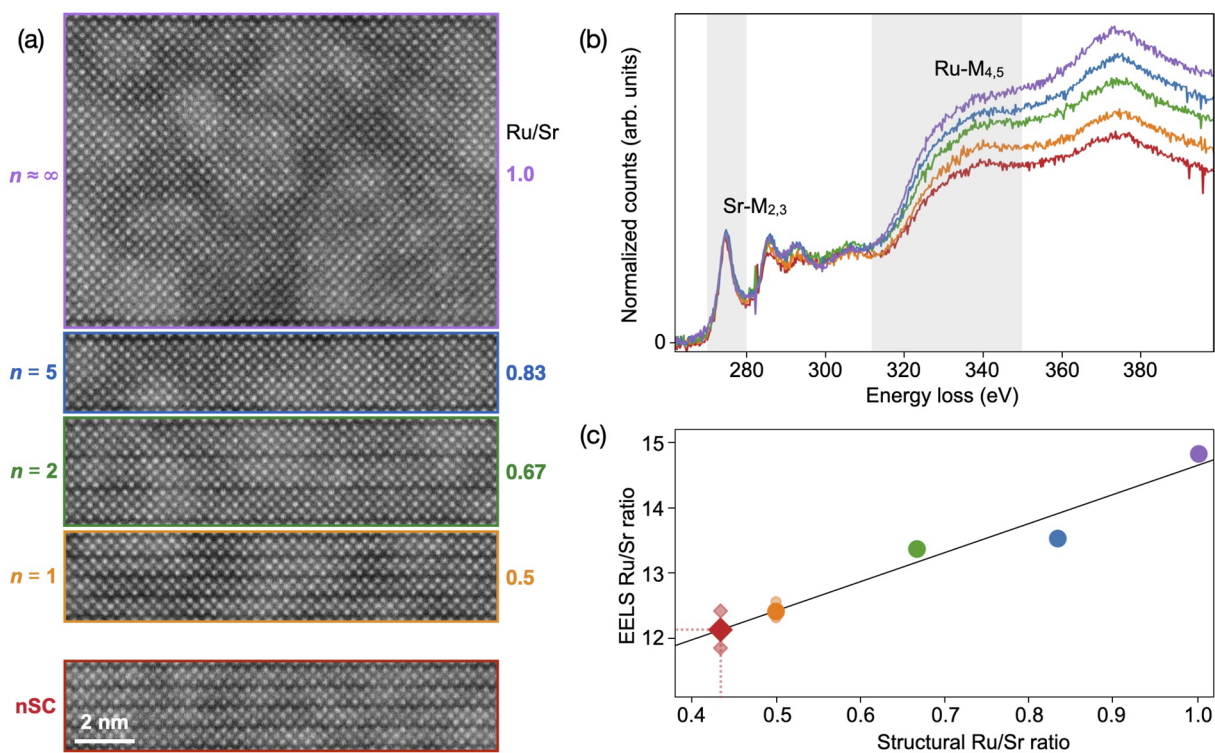


FIG. 3. (a) Atomic-resolution HAADF-STEM images of several different $Sr_{n+1}Ru_nO_{3n+1}$ Ruddlesden–Popper phase regions from the $T_c = 1.4$ K film identified by the structural n and nominal Ru/Sr ratio $n/(n+1)$. Also shown is a single apparently defect-free region of the non-superconducting Sr_2RuO_4 film (nSC). Additional contrast variations reflect the sensitivity of ruthenate compound to the high energy electron beam. (b) Local Sr- $M_{2,3}$ and Ru- $M_{4,5}$ EEL spectra from each region in (a), background subtracted and normalized to the intensity of the Sr- M_3 edge. Windows of integration used for each edge are shown in gray. (c) Structural Ru/Sr $n/(n+1)$ ratios vs integrated Ru/Sr EELS ratios for several acquisitions from different local n -phase regions including those shown in (a). Small markers for both the superconducting and the non-superconducting $n = 1$ phases show measurements of three distinct regions that were measured in each film. Regions from the superconducting film are assumed to have ideal stoichiometry. Circles denote regions from the superconducting film with $T_c = 1.4$ K; the diamond corresponds to the non-superconducting film. Large markers represent the average ratio measured for each phase. The black line is the calculated linear best fit for the measurements of the superconducting film. The measured EELS ratio for the non-superconducting film is used with this fit to estimate the relative Ru/Sr ratio (dotted red line).

Figure 3(a) shows atomic-resolution ADF-STEM images of several different Ruddlesden–Popper phase inclusions within the $T_c = 1.4$ K superconducting film. The structural Ruddlesden–Popper factor n is given to the right of each region, as well as the nominal Ru/Sr ratio calculated as $n/(n+1)$ to the left, with the top-most region approximated as $n = 24 \approx \infty$ for the purposes of this analysis. Especially in higher- n Ruddlesden–Popper systems, off-stoichiometry is accommodated by structural modifications that have clear signatures in STEM imaging.^{6,38,40} Through local spectroscopy by STEM-EELS, we isolate our measurements to include only the structural (and stoichiometric) phases of interest and infer the structural stoichiometry for each Ruddlesden–Popper region based on HAADF-STEM imaging. At the bottom of Fig. 3(a), an apparently defect-free $n = 1$ region of the non-superconducting (nSC) film is also shown, seemingly indistinguishable from the $n = 1$ regions of other superconducting samples. Spectroscopic measurements extracted from each of these regions in isolation contribute to a series of systematically varied spectra, which can be used to effectively quantify local Ru/Sr elemental stoichiometry.

Background-subtracted spectra of the Sr- $M_{2,3}$ and Ru- $M_{4,5}$ edges from each region in Fig. 3(a) are shown in Fig. 3(b), corresponding by color. All spectra are normalized by the summed integration of each Sr- M_3 edge. A clear trend emerges across the series, as the relative intensity of the Ru- $M_{4,5}$ edge grows with increasing n for each region, consistent with the relation given in Eq. (2). Notably, the spectrum from the non-superconducting sample (red spectrum) shows a relatively low Ru- $M_{4,5}$ intensity as compared to the nominally isostructural $n = 1$ region of the $T_c = 1.4$ K superconducting film (orange spectrum).

The trend relating the apparent structural Ru/Sr ratio with the measured relative strength of the ruthenium and strontium EELS signals for each region in the $T_c = 1.4$ K superconducting film can be quantified using Eq. (2). The strength of each edge (i.e., I_{Sr} , I_{Ru})

is measured by summing over the total intensity between 269–280 eV (Sr) and 313–350 eV (Ru) of the background subtracted spectra. Figure 3(c) shows the ratio of these integrations I_{Ru}/I_{Sr} plotted as a function of the presumed stoichiometry $[Ru]/[Sr] = n/(n+1)$ based on the Ruddlesden–Popper phase of each region. We thus extract the calibrated factor σ_B/σ_A with a linear best fit (shown by the black line).

With this calibration, the measured Ru/Sr EELS ratio I_{Ru}/I_{Sr} of the non-superconducting film can thus be used to estimate its actual relative Ru/Sr stoichiometry as ~ 0.43 (red dotted line). Compared to the expected ratio of 0.5 for the $n = 1$ superconducting phase, this measurement translates to ruthenium deficiency of $\sim 14\%$. In our analysis, we assume each region within the superconducting film contains no significant vacancies of any species. Consequently, the result of our quantification provides a lower bound on the actual ruthenium vacancies present in the non-superconducting film. Accounting for additional hypothetical ruthenium vacancies within the superconducting film would shift the calibration to smaller Ru/Sr ratios and indicate even higher vacancy density in the non-superconducting film. By comparison, high quality thin films of SrRuO₃ grown by MBE on (001) SrTiO₃ have been shown to accommodate up to 30% ruthenium vacancies with almost no detectable differences in traditional structural measurements by XRD, RHEED, or HAADF-STEM imaging.⁴¹ In these films, the RRR is a more reliable indicator of disorder introduced by ruthenium vacancies, reaching as high as 84.3 in the most perfect films^{42,47} and as low as five in highly deficient SrRu_{0.7}O₃ films⁴¹ (the RRR of the SrRuO₃ film used as a standard for our SEM-EDX measurements is 21.4).²⁷ This stoichiometric analysis also does not address the possibility of additional oxygen vacancies, which may further contribute to the atomic-scale disorder impacting superconductivity in these films.

In addition to elemental analysis, EELS also provides access to rich chemical information about local bonding environments via

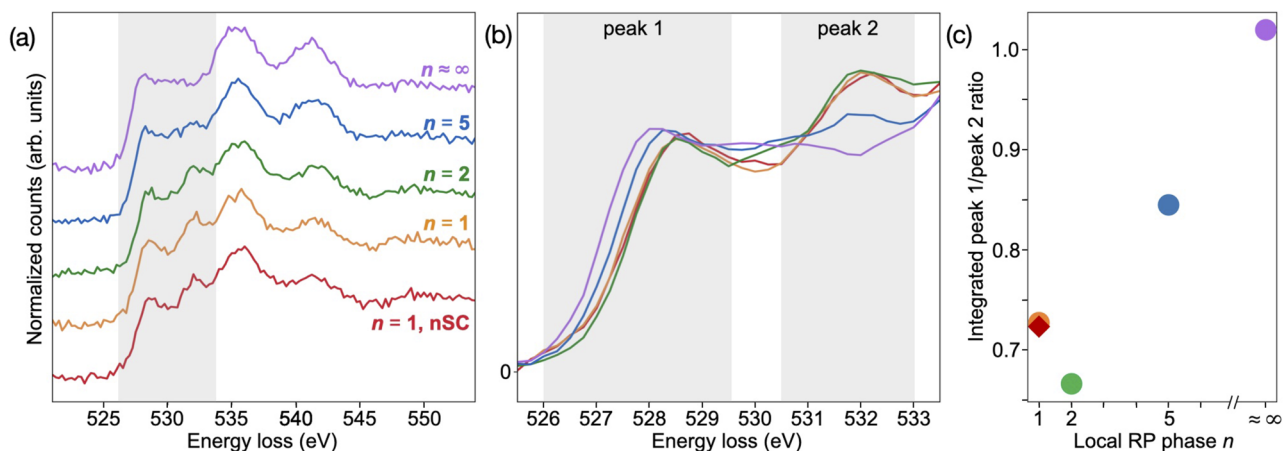


FIG. 4. (a) Local O–K EEL spectra from the same regions shown in Fig. 3(a), normalized, background-subtracted, and vertically offset for clarity. Highlighted in gray is the edge onset region that reflects transition metal $3d$ –oxygen $2p$ hybridization, replotted in (b). Spectra are renormalized to the energy range shown (526.5–533.5 eV), smoothed with a five-channel third-order Savitzky–Golay filter, and plotted on the same vertical scale for comparison between different local Ruddlesden–Popper phases. (c) Ratios of the integrated spectral weights of “peak 1” and “peak 2” labeled in (b) for each region. Circles denote regions from within the superconducting film with $T_c = 1.4$ K; the diamond corresponds to the non-superconducting film.

energy loss near-edge structure (ELNES).^{14,46,48,49} In the complex oxides, the O–K edge ELNES can be used to fingerprint a wide range of sample variations,⁵⁰ given its strong interaction with the transition metal and rare-earth sites. Figure 4(a) shows O–K edge spectra from the same regions studied in Fig. 3. The first ~5 eV of the O–K edge are generally ascribed to hybridization between oxygen and the transition metal,^{50,51} so any signatures of ruthenium vacancies would be expected near the edge onset. In a previous study, polarized x-ray absorption spectroscopy (XAS) revealed a response in this region of the spectrum reflecting the insulating character of highly ruthenium-deficient films.²⁵ Here, the density of ruthenium vacancies in our metallic non-superconducting film is presumably much lower, and no obvious distinction between the unpolarized O–K EELS edges from $n = 1$ regions of the superconducting and non-superconducting films is observed.

Further inspection of the complete series, however, does reveal significant spectroscopic variation across the Ruddlesden–Popper series, particularly in the 526–533 eV range shown magnified in Fig. 4(b). The two peaks highlighted reflect different local oxygen bonding configurations. Out-of-plane or apical Ru–O bonds are reflected mostly in peak 1, while in-plane Ru–O bonds contribute to both peaks 1 and 2.^{25,52,53} Fig. 4(c) illustrates the distinct spectroscopic signatures of different structural layers: in the low-dimensional phases (e.g., $n = 1$), the relative strength of in-plane to out-of-plane hybridization is stronger than in the more three-dimensional phases (e.g., $n \approx \infty$). Our local spectroscopic measurements enable us to separate the individual spectral contributions of these structural inhomogeneities.

IV. DISCUSSION

Given the role of the RuO₂ plane in Sr₂RuO₄ superconductivity, we conclude that the ruthenium vacancies identified and quantified by our study are linked to the suppression of superconductivity in ruthenium-poor films. Our results reveal a direct correlation between ruthenium deficiency and non-superconducting behavior and also suggest that ruthenium vacancies on the order of ~14% can occur in films of otherwise apparently high crystalline quality. Recent experiments by confocal micro-Raman spectroscopy in strongly ruthenium-deficient Sr₂RuO₄ thin films have proposed these take the form of ruthenium point vacancies (see Fig. S9 in the supplementary material),²⁵ but additional experiments through techniques such as positron annihilation lifetime spectroscopy (PALS) may contribute more insights. While our local measurements do not address possible macroscopic variations in stoichiometry across a single sample, they provide a quantitative benchmark of ruthenium deficiency levels for future studies of Sr₂RuO₄.

More broadly, our study illustrates a strategy for stabilizing desired properties within a specific Ruddlesden–Popper phase or other layered series. We discuss them here in the context of Sr₂RuO₄, but similar connections can easily be drawn to low- n Ruddlesden–Popper phases of other materials, which are of growing interest for superconductivity⁵⁴ and other functional properties.^{55–60}

As described by Nair *et al.*,²² the thermodynamic window for Sr₂RuO₄ thin film growth is quite narrow (see Fig. S10 in the supplementary material). In a simplified picture, the desired Sr₂RuO₄ structure—with corresponding Ru/Sr stoichiometry of 1/2—is achieved within this window. Small deviations in either

temperature or oxygen pressure, however, may yield samples with varying Ru/Sr ratios. Using Ru/Sr stoichiometry as the indicator, we thus consider three fundamental cases: (1) Ru/Sr = 1/2 (the “correct” Sr₂RuO₄ phase); (2) Ru/Sr >1/2 (ruthenium rich); and (3) Ru/Sr <1/2 (ruthenium poor).

The three films shown in Fig. 2 perfectly illustrate each of these possible cases for Sr₂RuO₄ thin films. The first (ideal) case, Ru/Sr = 1/2, produces a superconducting Sr₂RuO₄ film. The film shown in Fig. 2(c) shows a near-perfect Sr₂RuO₄ structure and indeed exhibits one of the highest reported T_c s at 1.8 K.

When perfectly ideal conditions are not yet established, however, it is necessary to consider the second and third cases. In case 2, a globally ruthenium-rich film shows a higher density of Sr _{$n+1$} Ru _{n} O _{$3n+1$} inclusions but also exhibits a clear superconducting transition at relatively high temperature ($T_c = 1.4$ K). When growth conditions stray outside the optimal window toward lower temperatures or lower oxygen pressure, excess ruthenium is accommodated through syntactic intergrowths of these higher- n Sr _{$n+1$} Ru _{n} O _{$3n+1$} phases with relatively little impact on the functional properties (i.e., superconductivity) of the film. The resulting mixed-phase film contains “enough” Sr₂RuO₄ layers to host superconductivity along a percolative transport path between these inert higher- n phases, thus demonstrating how the desired outcome (superconductivity) can still be realized even in a globally off-stoichiometric Ru/Sr >1/2 case. Similar stoichiometric accommodation has been described in Sr _{$n+1$} Ti _{n} O _{$3n+1$} dielectrics.^{6,38,40}

In case 3, the ruthenium poor side of the growth window proves less forgiving. Generally, Ruddlesden–Popper compounds with higher n can accommodate B -site deficient off-stoichiometry through the addition of extra rock salt (e.g., SrO) planes,^{38,40} which create regions of effectively lower local n . From the $n = 1$ phase, however, there is no accessible lower- n phase, so a similar mechanism is unavailable in Sr₂RuO₄. Instead, ruthenium vacancies seem to exist directly within the Sr₂RuO₄ structure, which are hidden to even advanced structural measurements but evident in certain spectroscopic probes. Thus, even though the non-superconducting film in Fig. 2(a) visibly retains a uniform structure of the Sr₂RuO₄ parent compound, the presence of ruthenium vacancies in the material suppresses superconductivity.

With these results, we have shown that for certain low- n Ruddlesden–Popper compounds it can be advantageous to err toward B -site rich conditions (rather than B -site deficient) within the thermodynamic growth window for the desired phase in order to take advantage of structural off-stoichiometric mitigation. Conversely, samples that appear structurally pristine but do not exhibit the desired or expected properties of an ordered phase may be inferred to host vacancy disorder similar to that revealed by our spectroscopic measurements. This wisdom may be extended to other layered oxides,⁶¹ such as the Aurivillius and Dion–Jacobson homologous series,⁶² with the appropriate adjustments by the limiting endmember cases.

V. CONCLUSION

In this study, we have disentangled the effects of two types of structural disorder for superconducting thin films of Sr₂RuO₄. We show that ruthenium rich samples can accommodate significant off-stoichiometry through the formation of local higher- n

$\text{Sr}_{n+1}\text{Ru}_n\text{O}_{3n+1}$ syntactic intergrowths with relatively little detriment to the superconducting T_c . Harnessing these higher phase Ruddlesden–Popper inclusions, we further create a self-contained reference series upon which to base quantitative, local EELS measurements of a non-superconducting Sr_2RuO_4 thin film, thereby revealing ruthenium vacancies hidden to other structural probes. We build upon previous qualitative work²⁵ and quantify the density of these vacancies at $\sim 14\%$, suggesting that ruthenium vacancies suppress superconducting behavior before impacting the overall Sr_2RuO_4 crystalline structure. Considering the narrow thermodynamic growth window for this compound,²² these conclusions provide insights to guide future successful growth of superconducting Sr_2RuO_4 and other Ruddlesden–Popper or homologous series materials.

SUPPLEMENTARY MATERIAL

Additional data and characterization relevant to this article and referenced in the main text—including Table 1 and Figs. S1–S10—are provided in the [supplementary material](#).

ACKNOWLEDGMENTS

This work was primarily supported by the NSF [Platform for the Accelerated Realization, Analysis, and Discovery of Interface Materials (PARADIM)] under Cooperative Agreement No. DMR-2039380. This research was funded, in part, by the Gordon and Betty Moore Foundation’s EPiQS Initiative (Grant No. GBMF9073) to Cornell University as well as NSF (Grant Nos. DMR-1709255 and DMR-2104427) and the Air Force Office of Scientific Research (AFOSR, Grant No. FA9550-21-1-0168). This work made use of the Cornell Center for Materials Research (CCMR) Shared Facilities, which are supported through the NSF MRSEC Program (Grant No. DMR-1719875). The FEI Titan Themis 300 was acquired through NSF-MRI-1429155, with additional support from Cornell University, the Weill Institute, and the Kavli Institute at Cornell. Substrate preparation was performed, in part, at the Cornell NanoScale Facility, a member of the National Nanotechnology Coordinated Infrastructure (NNCI), which is supported by the NSF (Grant No. NNCI-2025233).

AUTHOR DECLARATIONS

Conflict of Interest

The authors have no conflicts to disclose.

DATA AVAILABILITY

The data that support the findings of this study have been deposited in the Platform for the Accelerated Realization, Analysis, and Discovery of Interface Materials (PARADIM) database (<https://doi.org/10.34863/xvbs-ph84>).

REFERENCES

¹J. G. Bednorz and K. A. Müller, “Possible high T_c superconductivity in the Ba–La–Cu–O System,” *Z. Phys. B: Condens. Matter* **64**, 189–193 (1986).

²Y. Maeno, H. Hashimoto, K. Yoshida, S. Nishizaki, T. Fujita, J. G. Bednorz, and F. Lichtenberg, “Superconductivity in a layered perovskite without copper,” *Nature* **372**(6506), 532–534 (1994).

³D. Li, K. Lee, B. Y. Wang, M. Osada, S. Crossley, H. R. Lee, Y. Cui, Y. Hikita, and H. Y. Hwang, “Superconductivity in an infinite-layer nickelate,” *Nature* **572**(7771), 624–627 (2019).

⁴R. Ramesh and N. A. Spaldin, “Multiferroics: Progress and prospects in thin films,” *Nat. Mater.* **6**, 21–29 (2007).

⁵J. H. Lee, L. Fang, E. Vlahos, X. Ke, Y. W. Jung, L. F. Kourkoutis, J.-W. Kim, P. J. Ryan, T. Heeg, M. Roeckerath, V. Goian, M. Bernhagen, R. Uecker, P. C. Hammel, K. M. Rabe, S. Kamba, J. Schubert, J. W. Freeland, D. A. Muller, C. J. Fennie, P. Schiffer, V. Gopalan, E. Johnston-Halperin, and D. G. Schlom, “A Strong Ferroelectric Ferromagnet Created by means of Spin-Lattice Coupling,” *Nature* **466**, 954–958 (2010).

⁶C.-H. Lee, N. D. Orloff, T. Birol, Y. Zhu, V. Goian, E. Rocas, R. Haislmaier, E. Vlahos, J. A. Mundy, L. F. Kourkoutis, Y. Nie, M. D. Biegalski, J. Zhang, M. Bernhagen, N. A. Benedek, Y. Kim, J. D. Brock, R. Uecker, X. X. Xi, V. Gopalan, D. Nuzhnyy, S. Kamba, D. A. Muller, I. Takeuchi, J. C. Booth, C. J. Fennie, and D. G. Schlom, “Exploiting dimensionality and defect mitigation to create tunable microwave dielectrics,” *Nature* **502**(7472), 532–536 (2013).

⁷A. Bhattacharya and S. J. May, “Magnetic oxide heterostructures,” *Annu. Rev. Mater. Res.* **44**, 65–90 (2014).

⁸Y. Moritomo, A. Asamitsu, H. Kuwahara, and Y. Tokura, “Giant magnetoresistance of manganese oxides with a layered perovskite structure,” *Nature* **380**(6570), 141–144 (1996).

⁹M. Bosman, V. J. Keast, J. L. García-Muñoz, A. J. D’Alfonso, S. D. Findlay, and L. J. Allen, “Two-dimensional mapping of chemical information at atomic resolution,” *Phys. Rev. Lett.* **99**(8), 086102 (2007).

¹⁰K. Kimoto, T. Asaka, T. Nagai, M. Saito, Y. Matsui, and K. Ishizuka, “Element-selective imaging of atomic columns in a crystal using STEM and EELS,” *Nature* **450**(7170), 702–704 (2007).

¹¹D. A. Muller, L. F. Kourkoutis, M. Murfitt, J. H. Song, H. Y. Hwang, J. Silcox, N. Dellby, and O. L. Krivanek, “Atomic-scale chemical imaging of composition and bonding by aberration-corrected microscopy,” *Science* **319**(5866), 1073–1076 (2008).

¹²R. F. Egerton, “Electron energy-loss spectroscopy in the TEM,” *Rep. Prog. Phys.* **72**(1), 016502 (2008).

¹³E. J. Monkman, C. Adamo, J. A. Mundy, D. E. Shai, J. W. Harter, D. Shen, B. Burganov, D. A. Muller, D. G. Schlom, and K. M. Shen, “Quantum many-body interactions in digital oxide superlattices,” *Nat. Mater.* **11**(10), 855–859 (2012).

¹⁴G. Botton and S. Prabhudev, in *Analytical Electron Microscopy*, edited by P. W. Hawkes and J. C. H. Spence (Springer Handbooks, 2019), pp. 345–453.

¹⁵A. P. Mackenzie, T. Scaffidi, C. W. Hicks, and Y. Maeno, “Even odder after twenty-three years: The superconducting order parameter puzzle of Sr_2RuO_4 ,” *npj Quantum Mater.* **2**(1), 40 (2017).

¹⁶A. Garg, M. Randeria, and N. Trivedi, “Strong correlations make high-temperature superconductors robust against disorder,” *Nat. Phys.* **4**(10), 762–765 (2008).

¹⁷A. P. Mackenzie, R. K. W. Haselwimmer, A. W. Tyler, G. G. Lonzarich, Y. Mori, S. Nishizaki, and Y. Maeno, “Extremely strong dependence of superconductivity on disorder in Sr_2RuO_4 ,” *Phys. Rev. Lett.* **80**(1), 161–164 (1998).

¹⁸Z. Q. Mao, Y. Mori, and Y. Maeno, “Suppression of superconductivity in Sr_2RuO_4 caused by defects,” *Phys. Rev. B* **60**(1), 610–614 (1999).

¹⁹Y. Krockenberger, M. Uchida, K. S. Takahashi, M. Nakamura, M. Kawasaki, and Y. Tokura, “Growth of superconducting Sr_2RuO_4 thin films,” *Appl. Phys. Lett.* **97**(8), 082502 (2010).

²⁰J. Cao, D. Massarotti, M. E. Vickers, A. Kursumovic, A. Di Bernardo, J. W. A. Robinson, F. Tafuri, J. L. MacManus-Driscoll, and M. G. Blamire, “Enhanced localized superconductivity in Sr_2RuO_4 thin film by pulsed laser deposition,” *Supercond. Sci. Technol.* **29**(9), 095005 (2016).

²¹M. Uchida, M. Ide, H. Watanabe, K. S. Takahashi, Y. Tokura, and M. Kawasaki, “Molecular beam epitaxy growth of superconducting Sr_2RuO_4 films,” *APL Mater.* **5**(10), 106108 (2017).

²²H. P. Nair, J. P. Ruf, J. P. Ruf, N. J. Schreiber, L. Miao, M. L. Grandon, D. J. Baek, B. H. Goodge, J. P. C. Ruff, L. F. Kourkoutis, K. M. Shen, and D. G. Schlom,

- "Demystifying the growth of superconducting Sr_2RuO_4 thin films," *APL Mater.* **6**(10), 101108 (2018).
- ²³S. N. Ruddlesden and P. Popper, "The compound $\text{Sr}_3\text{Ti}_2\text{O}_7$ and its structure," *Acta Crystallogr.* **11**(1), 54–55 (1958).
- ²⁴T. Williams, F. Lichtenberg, A. Reller, and G. Bednorz, "New layered perovskites in the Sr–Ru–O system: A transmission electron microscope study," *Mater. Res. Bull.* **26**(8), 763–770 (1991).
- ²⁵G. Kim, Y. Eren Suyolcu, J. Herrero-Martin, D. Putzky, H. P. Nair, J. P. Ruf, N. J. Schreiber, C. Dietl, G. Christiani, G. Logvenov, M. Minola, P. A. van Aken, K. M. Shen, D. G. Schlom, and B. Keimer, "Electronic and vibrational signatures of ruthenium vacancies in Sr_2RuO_4 thin films," *Phys. Rev. Mater.* **3**(9), 094802 (2019).
- ²⁶H. P. Nair, Y. Liu, J. P. Ruf, N. J. Schreiber, S.-L. Shang, D. J. Baek, B. H. Goodge, L. F. Kourkoutis, Z.-K. Liu, K. M. Shen, and D. G. Schlom, "Synthesis science of SrRuO_3 and CaRuO_3 epitaxial films with high residual resistivity ratios," *APL Mater.* **6**(4), 046101 (2018).
- ²⁷L. Miao, N. J. Schreiber, H. P. Nair, B. H. Goodge, S. Jiang, J. P. Ruf, Y. Lee, M. Fu, B. Tsang, Y. Li, J. Shan, K. Fai Mak, L. F. Kourkoutis, D. G. Schlom, and K. M. Shen, "Strain relaxation induced transverse resistivity anomalies in SrRuO_3 thin films," *Phys. Rev. B* **102**(6), 064406 (2020).
- ²⁸H. C. Montgomery, "Method for measuring electrical resistivity of anisotropic materials," *J. Appl. Phys.* **42**(7), 2971–2975 (1971).
- ²⁹I. Miccoli, F. Edler, H. Pfnür, and C. Tegenkamp, "The 100th anniversary of the four-point probe technique: The role of probe geometries in isotropic and anisotropic systems," *J. Phys.: Condens. Matter* **27**(22), 223201 (2015).
- ³⁰Y. Maeno, T. Ando, Y. Mori, E. Ohmichi, S. Ikeda, S. NishiZaki, and S. Nakatsuji, "Enhancement of superconductivity of Sr_2RuO_4 to 3 K by embedded metallic microdomains," *Phys. Rev. Lett.* **81**(17), 3765–3768 (1998).
- ³¹S. S. Ghosh, Y. Xin, Z. Mao, and E. Manousakis, "Interface between Sr_2RuO_4 and Ru-metal inclusion: Implications for its superconductivity," *Physical Review B* **96**(18), 184506 (2017).
- ³²B. H. Goodge, D. J. Baek, and L. F. Kourkoutis, "Atomic-resolution elemental mapping at cryogenic temperatures enabled by direct electron detection," *arXiv:2007.09747* (2020).
- ³³P. Cueva, R. Hovden, J. A. Mundy, H. L. Xin, and D. A. Muller, "Data processing for atomic resolution electron energy loss spectroscopy," *Microsc. Microanal.* **18**, 667–675 (2012).
- ³⁴J. Kim, J. Mun, C. M. Palomares García, B. Kim, R. S. Perry, Y. Jo, H. Im, H. G. Lee, E. K. Ko, S. H. Chang, S. B. Chung, M. Kim, J. W. A. Robinson, S. Yonezawa, Y. Maeno, L. Wang, and T. W. Noh, "Superconducting Sr_2RuO_4 thin films without out-of-phase boundaries by higher-order Ruddlesden–Popper intergrowth," *Nano Lett.* **21**(10), 4185–4192 (2021).
- ³⁵M. A. Zurbuchen, Y. Jia, S. Knapp, A. H. Carim, D. G. Schlom, and X. Q. Pan, "Defect generation by preferred nucleation in epitaxial $\text{Sr}_2\text{RuO}_4/\text{LaAlO}_3$," *Appl. Phys. Lett.* **83**(19), 3891–3893 (2003).
- ³⁶Y. Fang, H. P. Nair, L. Miao, B. H. Goodge, N. J. Schreiber, J. P. Ruf, L. F. Kourkoutis, K. M. Shen, D. G. Schlom, and B. J. Ramshaw, "Quantum oscillations and quasiparticle properties of thin film Sr_2RuO_4 ," *Phys. Rev. B* **104**, 045152 (2021).
- ³⁷R. Fittipaldi, A. Vecchione, R. Ciancio, S. Pace, M. Cuoco, D. Stornaiuolo, D. Born, F. Tafuri, E. Olsson, S. Kittaka, H. Yaguchi, and Y. Maeno, "Superconductivity in Sr_2RuO_4 - $\text{Sr}_3\text{Ru}_2\text{O}_7$ eutectic crystals," *EPL* **83**(2), 27007 (2008).
- ³⁸N. M. Dawley, B. H. Goodge, W. Egger, M. R. Barone, L. F. Kourkoutis, D. J. Keeble, and D. G. Schlom, "Defect accommodation in off-stoichiometric $(\text{SrTiO}_3)_n\text{SrO}$ Ruddlesden–Popper superlattices studied with positron annihilation spectroscopy," *Appl. Phys. Lett.* **117**(6), 062901 (2020).
- ³⁹Z. Q. Mao, Y. Maeno, and H. Fukazawa, "Crystal growth of Sr_2RuO_4 ," *Mater. Res. Bull.* **35**(11), 1813–1824 (2000).
- ⁴⁰C. M. Brooks, L. F. Kourkoutis, T. Heeg, J. Schubert, D. A. Muller, and D. G. Schlom, "Growth of homoepitaxial SrTiO_3 thin films by molecular-beam epitaxy," *Appl. Phys. Lett.* **94**(16), 162905 (2009).
- ⁴¹Y. K. Wakabayashi, S. Kaneta-Takada, Y. Krockenberger, K. Takiguchi, S. Ohya, M. Tanaka, Y. Taniyasu, and H. Yamamoto, "Structural and transport properties of highly Ru-deficient $\text{SrRu}_{0.7}\text{O}_3$ thin films prepared by molecular beam epitaxy: Comparison with stoichiometric SrRuO_3 ," *AIP Adv.* **11**(3), 035226 (2021).
- ⁴²S. Kaneta-Takada, Y. K. Wakabayashi, Y. Krockenberger, S. Ohya, M. Tanaka, Y. Taniyasu, and H. Yamamoto, "Thickness-dependent quantum transport of Weyl fermions in ultra-high-quality SrRuO_3 films," *Appl. Phys. Lett.* **118**(9), 092408 (2021).
- ⁴³M. J. Olszta, J. Wang, and E. C. Dickey, "Stoichiometry and valence measurements of niobium oxides using electron energy-loss spectroscopy," *J. Microsc.* **224**(3), 233–241 (2006).
- ⁴⁴L. Lajaunie, F. Boucher, R. Dessapt, and P. Moreau, "Quantitative use of electron energy-loss spectroscopy Mo- $M_{2,3}$ edges for the study of molybdenum oxides," *Ultramicroscopy* **149**, 1–8 (2015).
- ⁴⁵D. A. Muller, D. J. Singh, and J. Silcox, "Connections between the electron-energy-loss spectra, the local electronic structure, and the physical properties of a material: A study of nickel aluminum alloys," *Phys. Rev. B* **57**(14), 8181 (1998).
- ⁴⁶R. F. Egerton, *Electron Energy-Loss Spectroscopy in the Electron Microscope* (Springer, Boston, MA, 2011).
- ⁴⁷K. Takiguchi, Y. K. Wakabayashi, H. Irie, Y. Krockenberger, T. Otsuka, H. Sawada, S. A. Nikolaev, H. Das, M. Tanaka, Y. Taniyasu, and H. Yamamoto, "Quantum transport evidence of Weyl fermions in an epitaxial ferromagnetic oxide," *Nat. Commun.* **11**(1), 4969 (2020).
- ⁴⁸A. Ohtomo, D. A. Muller, J. L. Grazul, and H. Y. Hwang, "Artificial charge-modulation in atomic-scale perovskite titanate superlattices," *Nature* **419**(6905), 378–380 (2002).
- ⁴⁹D. A. Muller, Y. Tzou, R. Raj, and J. Silcox, "Mapping sp^2 and sp^3 states of carbon at sub-nanometre spatial resolution," *Nature* **366**(6457), 725–727 (1993).
- ⁵⁰L. Fitting Kourkoutis, H. L. Xin, T. Higuchi, Y. Hotta, J. H. Lee, Y. Hikita, D. G. Schlom, H. Y. Hwang, and D. A. Muller, "Atomic-resolution spectroscopic imaging of oxide interfaces," *Philos. Mag.* **90**(35–36), 4731–4749 (2010).
- ⁵¹F. M. F. de Groot, M. Grioni, J. C. Fuggle, J. Ghijsen, G. A. Sawatzky, and H. Petersen, "Oxygen 1s x-ray-absorption edges of transition-metal oxides," *Phys. Rev. B* **40**(8), 5715–5723 (1989).
- ⁵²M. Schmidt, T. R. Cummins, M. Bürk, D. H. Lu, N. Nücker, S. Schuppler, and F. Lichtenberg, "Nature of the electronic states in the layered perovskite noncuprate superconductor Sr_2RuO_4 ," *Phys. Rev. B* **53**(22), R14761 (1996).
- ⁵³S. J. Moon, M. W. Kim, K. W. Kim, Y. S. Lee, J.-Y. Kim, J.-H. Park, B. J. Kim, S.-J. Oh, S. Nakatsuji, Y. Maeno, and I. Nagai, S. I. Ikeda, G. Cao, and T. W. Noh, "Electronic structures of layered perovskite Sr_2MO_4 ($M = \text{Ru}, \text{Rh}$, and Ir)," *Phys. Rev. B* **74**(11), 113104 (2006).
- ⁵⁴G. A. Pan, D. F. Segedin, H. LaBollita, Q. Song, E. M. Nica, B. H. Goodge, A. T. Pierce, S. Doyle, S. Novakov, D. C. Carrizales, A. T. N'Diaye, P. Shafer, H. Paik, J. T. Heron, J. A. Mason, A. Yacoby, L. F. Kourkoutis, O. Erten, C. M. Brooks, A. S. Botana, and J. A. Mundy, "Superconductivity in a quintuple-layer square-planar nickelate," *Nat. Mater.* **21**, 160–164 (2022).
- ⁵⁵B. Liu, X. Q. Liu, and X. M. Chen, " $\text{Sr}_2\text{LaAlTiO}_7$: A new Ruddlesden–Popper compound with excellent microwave dielectric properties," *J. Mater. Chem. C* **4**(8), 1720–1726 (2016).
- ⁵⁶J. A. Mundy, C. M. Brooks, M. E. Holtz, J. A. Moyer, H. Das, A. F. Rébola, J. T. Heron, J. D. Clarkson, S. M. Disseler, Z. Liu, A. Farhan, R. Held, R. Hovden, E. Padgett, Q. Mao, H. Paik, R. Misra, L. F. Kourkoutis, E. Arenholz, A. Scholl, J. A. Borchers, W. D. Ratcliff, R. Ramesh, C. J. Fennie, P. Schiffer, D. A. Muller, and D. G. Schlom, "Atomically engineered ferroic layers yield a room-temperature magnetoelectric multiferroic," *Nature* **537**(7621), 523–527 (2016).
- ⁵⁷S. Yoshida, H. Akamatsu, R. Tsuji, O. Hernandez, H. Padmanabhan, A. Sen Gupta, A. S. Gibbs, K. Mibu, S. Murai, J. M. Rondinelli, V. Gopalan, K. Tanaka, and K. Fujita, "Hybrid improper ferroelectricity in $(\text{Sr},\text{Ca})_3\text{Sn}_2\text{O}_7$ and beyond: Universal relationship between ferroelectric transition temperature and tolerance factor in $n = 2$ Ruddlesden–Popper phases," *J. Am. Chem. Soc.* **140**(46), 15690–15700 (2018).
- ⁵⁸K. Boulahya, D. Muñoz-Gil, A. Gómez-Herrero, M. T. Azcondo, and U. Amador, " $\text{Eu}_2\text{SrCo}_{1.5}\text{Fe}_{0.5}\text{O}_7$ a new promising Ruddlesden–Popper member as a cathode component for intermediate temperature solid oxide fuel cells," *J. Mater. Chem. A* **7**(10), 5601–5611 (2019).
- ⁵⁹Q. Wang, J. Hou, Y. Fan, X.-a. Xi, J. Li, Y. Lu, G. Huo, L. Shao, X.-Z. Fu, and J.-L. Luo, " $\text{Pr}_2\text{BaNiMnO}_{7-8}$ double-layered Ruddlesden–Popper perovskite

oxides as efficient cathode electrocatalysts for low temperature proton conducting solid oxide fuel cells," *J. Mater. Chem. A* **8**(16), 7704–7712 (2020).

⁶⁰N. M. Dawley, E. K. Pek, C.-H. Lee, E. J. Ragasa, X. Xiong, K. Lee, S. R. Phillpot, A. V. Chernatynskiy, D. G. Cahill, and D. G. Schlom, "Thermal conductivity of the $n = 1$ –5 and 10 members of the $(\text{SrTiO}_3)_n\text{SrO}$ Ruddlesden–Popper superlattices," *Appl. Phys. Lett.* **118**(9), 091904 (2021).

⁶¹C. Delmas, C. Fouassier, and P. Hagenmuller, "Structural classification and properties of the layered oxides," *Physica B+C* **99**(1-4), 81–85 (1980).

⁶²M. A. Zurbuchen, W. Tian, X. Q. Pan, D. Fong, S. K. Streiffer, M. E. Hawley, J. Lettieri, Y. Jia, G. Asayama, S. J. Fulk, D. J. Comstock, S. Knapp, A. H. Carim, and D. G. Schlom, "Morphology, structure, and nucleation of out-of-phase boundaries (OPBs) in epitaxial films of layered oxides," *J. Mater. Res.* **22**(6), 1439–1471 (2007).

Supplementary Information for ‘Disentangling types of lattice disorder impacting superconductivity in Sr₂RuO₄ by quantitative local probes’

Berit H. Goodge,^{1, a)} Hari P. Nair,² David J. Baek,³ Nathaniel J. Schreiber,² Ludi Miao,⁴ Jacob P. Ruf,^{4, 5} Emily N. Waite,^{6, 7} Philip M. Carubia,² Kyle M. Shen,^{4, 8} Darrell G. Schlom,^{2, 8, 9} and Lena F. Kourkoutis^{6, 8, b)}

¹⁾ *of Applied and Engineering Physics, Cornell University, Ithaca, NY 14853*

²⁾ *Department of Materials Science and Engineering, Cornell University, Ithaca, NY 14853*

³⁾ *School of Electrical and Computer Engineering, Cornell University, Ithaca, NY 14853*

⁴⁾ *Department of Physics, Cornell University, Ithaca, NY 14853*

⁵⁾ *current address: Max Planck Institute for Chemical Physics of Solids, 01187 Dresden, Germany*

⁶⁾ *School of Applied and Engineering Physics, Cornell University, Ithaca, NY 14853*

⁷⁾ *current address: Department of Physics and Frederick Seitz Materials Research Laboratory, University of Illinois, Urbana, Illinois 61801, USA*

⁸⁾ *Kavli Institute at Cornell for Nanoscale Science, Cornell University, Ithaca, NY 14853*

⁹⁾ *Leibniz-Institut für Kristallzüchtung, Max-Born-Str. 2, 12489 Berlin, Germany*

(Dated: 6 March 2022)

^{a)} Correspondence to bhg37@cornell.edu

^{b)} Correspondence to lena.f.kourkoutis@cornell.edu

T_c	Sr flux (atoms/cm ²)	Ru flux (atoms/cm ²)	O ₃ pressure (Torr)	Substrate temperature (°C)
non-superconducting	2.20×10^{13}	1.37×10^{13}	1.0×10^{-6}	910
1.4 K	1.85×10^{13}	1.31×10^{13}	9.6×10^{-7}	895-910
1.8 K	2.61×10^{13}	2.38×10^{13}	1.8×10^{-6}	900

TABLE S1. Growth conditions for the three Sr₂RuO₄ films studied here. Strontium and ruthenium fluxes are measured with a quartz crystal microbalance (QCM) inserted at the position of the substrate. The strontium flux is measured at the start of the growth day with negligible drift over time under normal circumstances. The fluxes reported here are calibrated from the measured QCM flux via comparison to the resulting film thickness measured by XRD. Ruthenium is evaporated from an electron beam evaporator and the flux is monitored by the aforementioned QCM as well as by electron impact emission spectroscopy (EIES) near the electron beam evaporator. Power to the electron beam is manually adjusted to maintain a constant EIES reading to achieve a stable ruthenium flux at the substrate. Excess ruthenium evaporates as RuO_x gas within the adsorption-controlled growth window. Ozone is introduced into the growth chamber by an ozone nozzle providing a mixture composed of ~ 80% O₃ and 20% O₂. The local enrichment of ozone pressure is calculated from the distance from the ozone nozzle to the substrate and the background chamber pressure. The background chamber pressure is measured using an ion gauge calibrated to oxygen. At the ion gauge the gas mix is assumed to be all oxygen, i.e., all the O₃ has broken down into O₂. Substrate temperatures during growth were measured using a pyrometer operating at 1550 nm.

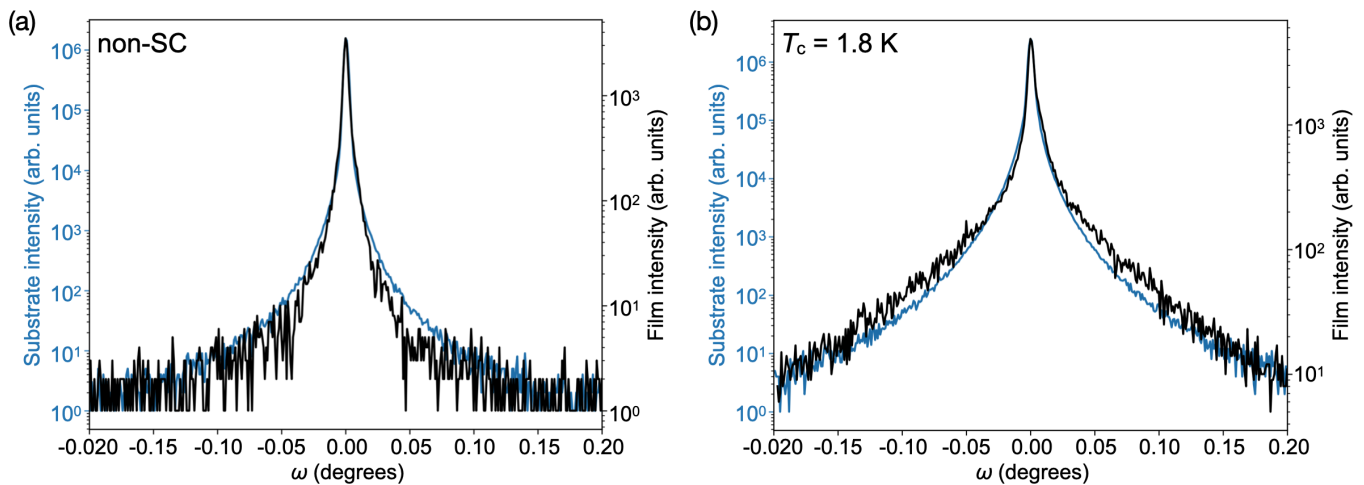


FIG. S1. Rocking curve measurements around the 006 reflection of the Sr₂RuO₄ film and the 220 reflection of the NdGaO₃ substrate for (a) non-superconducting and (b) $T_c = 1.8$ K films. In both cases, the full width at half maximum (FWHM) of each film is comparable to that of its substrate indicating high structural quality. (b) is reproduced from Nair, et al.¹

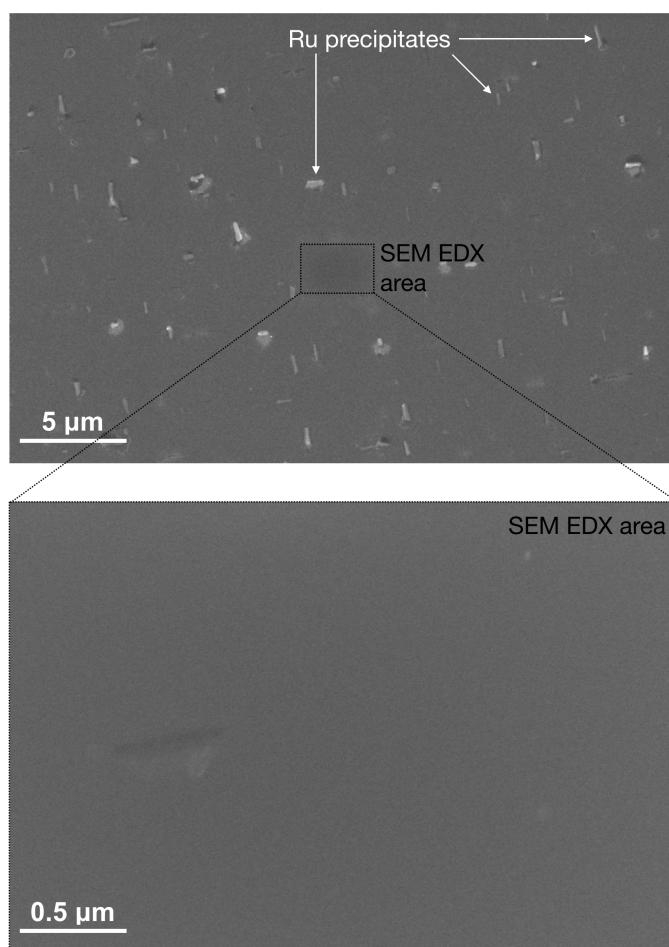


FIG. S2. Representative area of the Sr_2RuO_4 films analyzed by SEM-EDX. Large fields of view show mesoscopic ruthenium precipitates in the film. SEM-EDX measurements are localized as much as possible to limit signals from these inhomogeneities. Similarly, STEM lamellae prepared by FIB are extracted to avoid precipitates when possible.

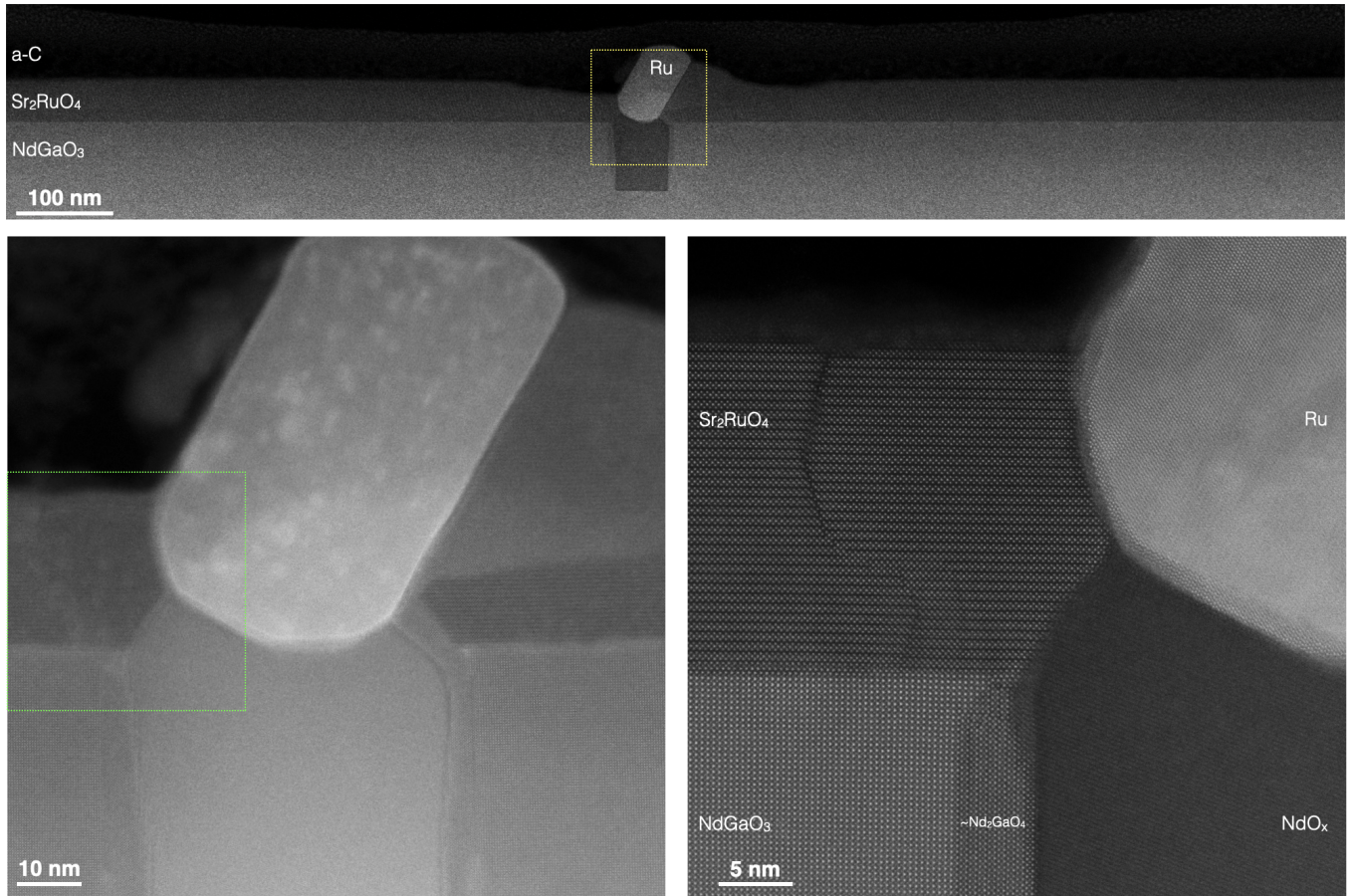


FIG. S3. HAADF-STEM microstructural characterization of a Ru-metal precipitate in a thin film of Sr_2RuO_4 . The highest magnification image at the bottom right comes from the region outlined by the dotted green box at left, which in turn shows a zoomed-in view of the dotted yellow box in the top panel. Small particulates of Ru metal are likely expelled from the Ru source during the adsorption-controlled growth, landing on the substrate surface. Here, the Ru metal appears to have reacted locally with the NdGaO_3 substrate, forming a small region of depleted material, likely NdO_x based on local spectral analysis. The Sr_2RuO_4 film grows around the inclusion, with only minor structural disruptions nearby. Spectroscopically, the Sr_2RuO_4 film near the inclusion is indistinguishable from clean crystalline regions far from such defects. Precipitates such as these are observed in both superconducting and non-superconducting films

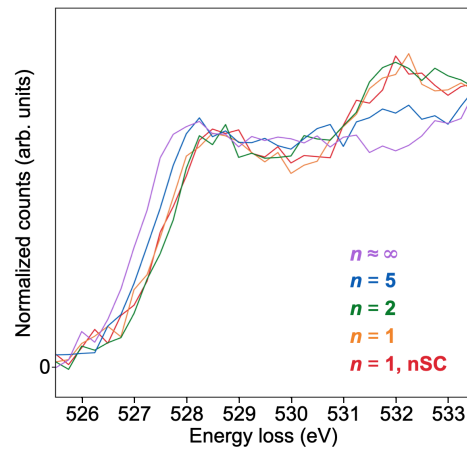


FIG. S4. Unfiltered reproduction of the spectra shown in Figure 4b of the main text.

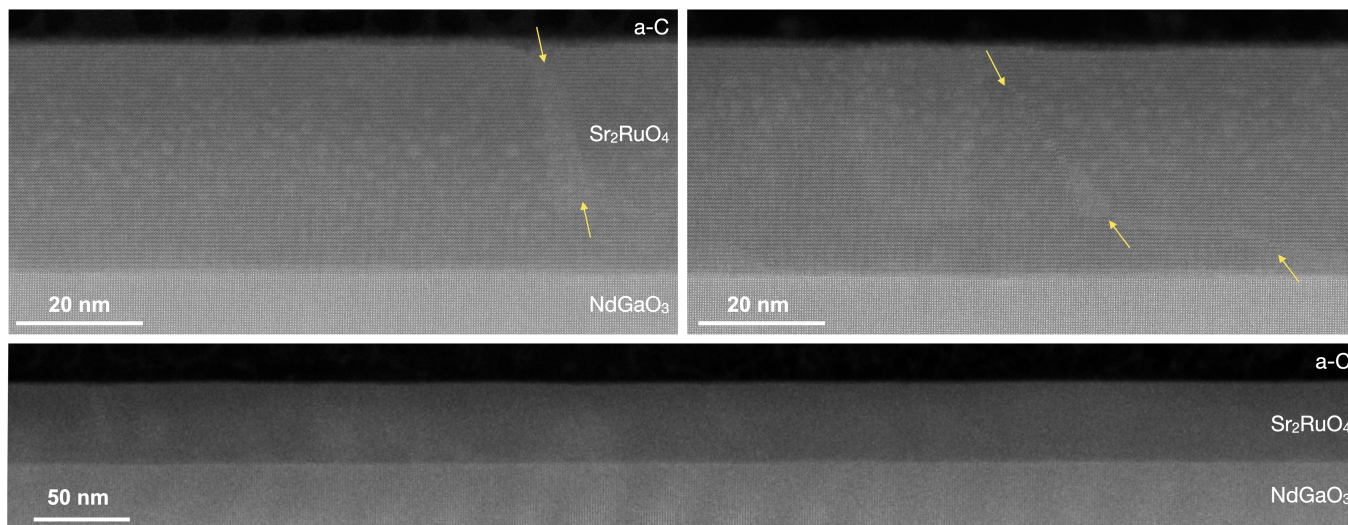


FIG. S5. Overview HAADF-STEM images of the non-superconducting film, showing sparse occurrence of extended defects within the film. Similar defect structures have been observed at higher densities in non-superconducting films^{2,3} and at similar densities in superconducting films.⁴

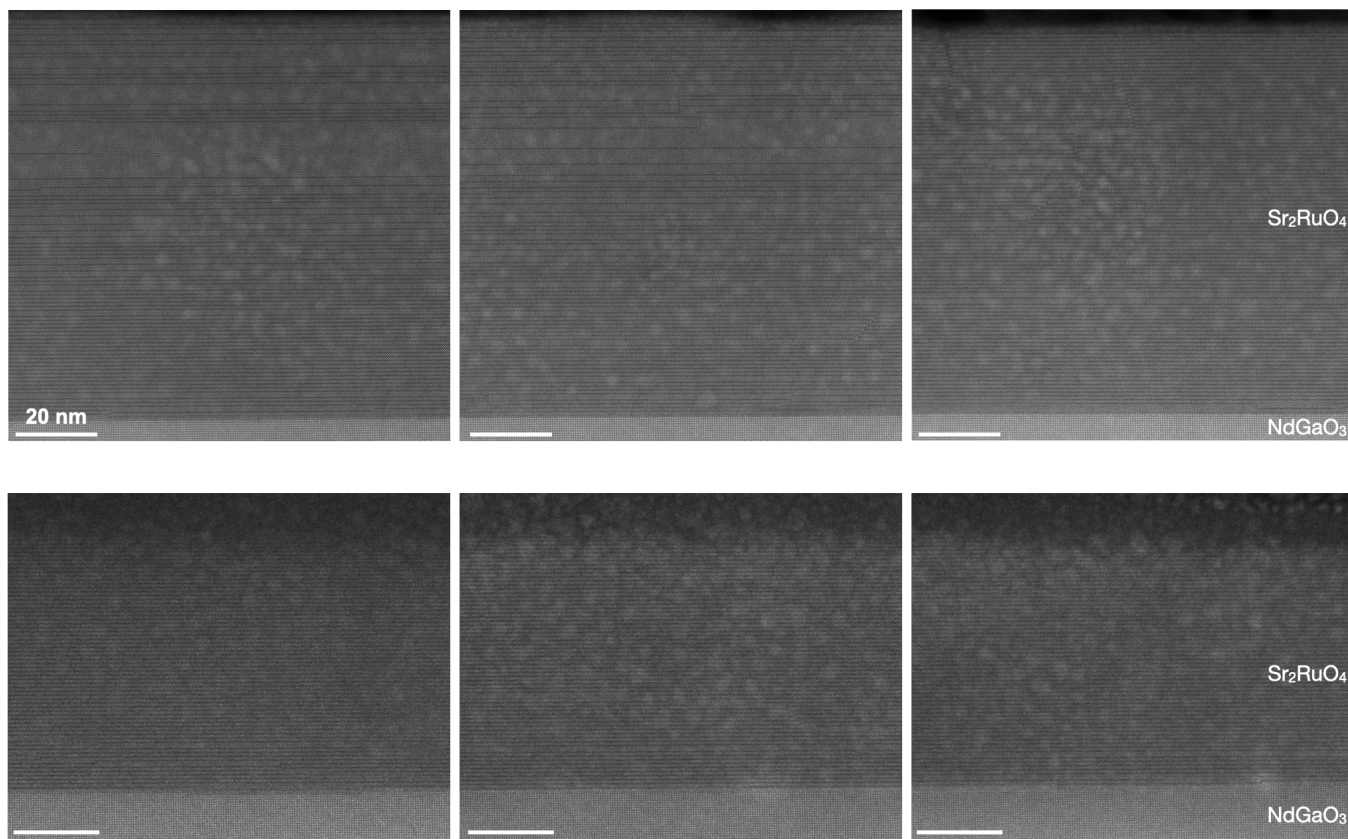


FIG. S6. Representative HAADF-STEM images showing the mixed-phase microstructure in the two superconducting films with (top) $T_c = 1.4$ K and (bottom) $T_c = 1.8$ K. All scale bars are 20 nm. The damage along the top surface of the $T_c = 1.8$ K film is a consequence sample preparation in the FIB. The white patches observed in both films are due to electron beam exposure.

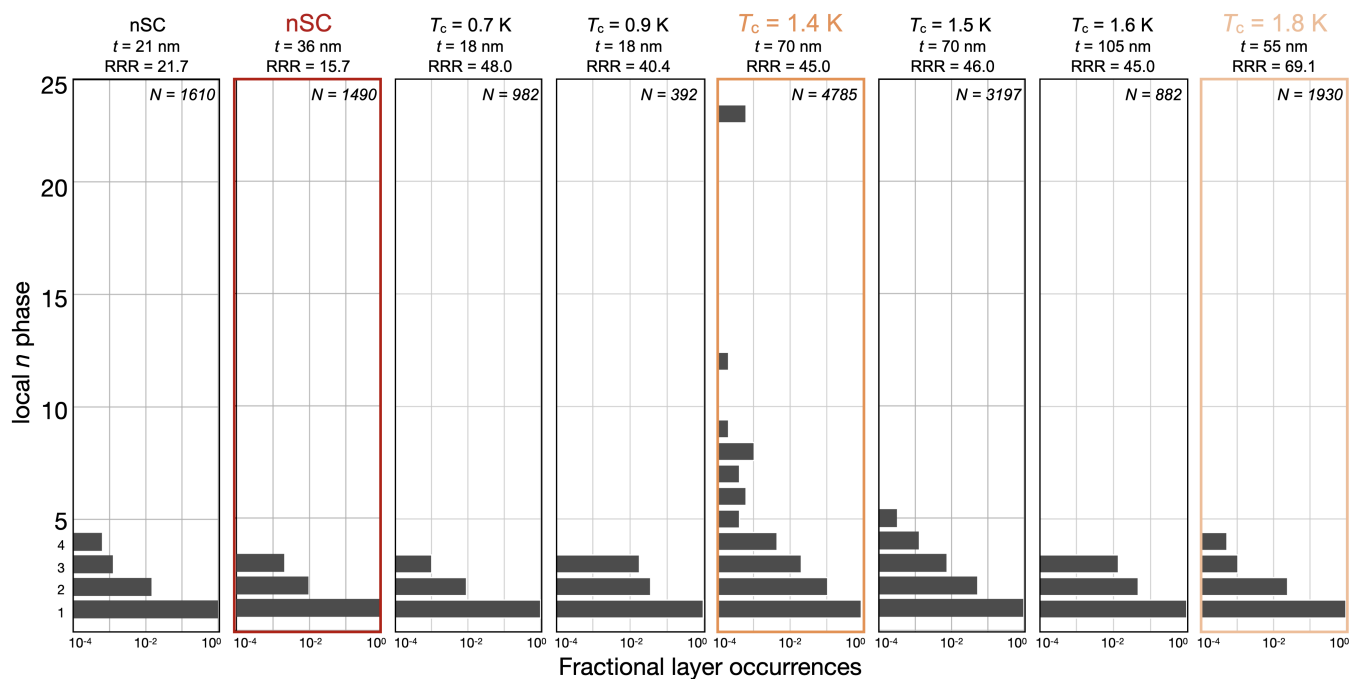


FIG. S7. Histograms comparing the occurrence of different n phases counted from HAADF-STEM images of several Sr_2RuO_4 thin films. The numbers of occurrences are normalized by the total number of layers counted in each film (N); note that the occurrences are plotted on a log scale. The transition temperature T_c is given for films that superconduct; non-superconducting films are labelled “nSC”. The thickness t of each film is also indicated. The three films studied in depth in this report are outlined by colored boxes. Superconductivity is not limited only to thick films, as evidenced by the two superconducting 18 nm-thick films.

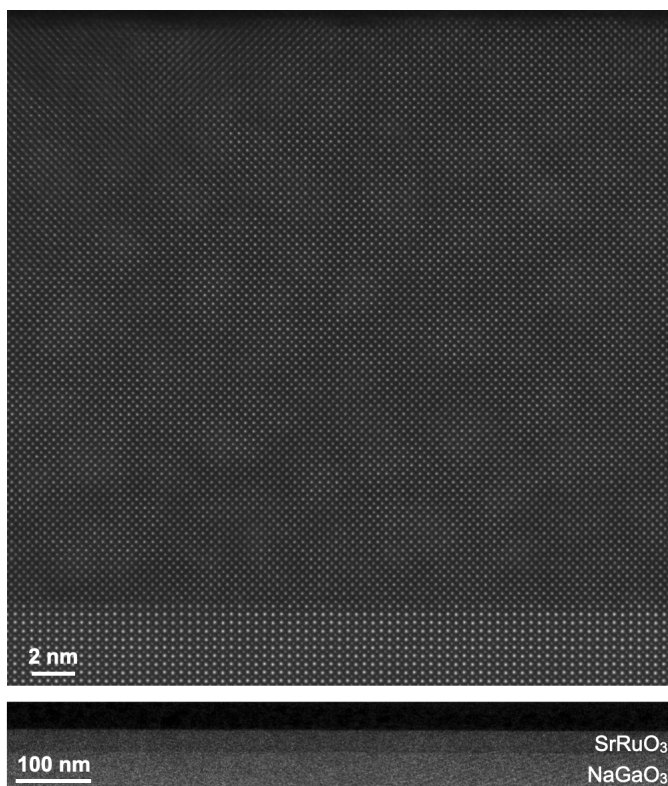


FIG. S8. HAADF-STEM images of the 30 nm thick SrRuO₃ film on (110) NdGaO₃ referenced in the SEM-EDX measurements show no obvious inclusions of RuO₂ or ruthenium metal precipitates or other secondary phases. The film's RRR of 21.4 indicates fairly low levels of disorder.

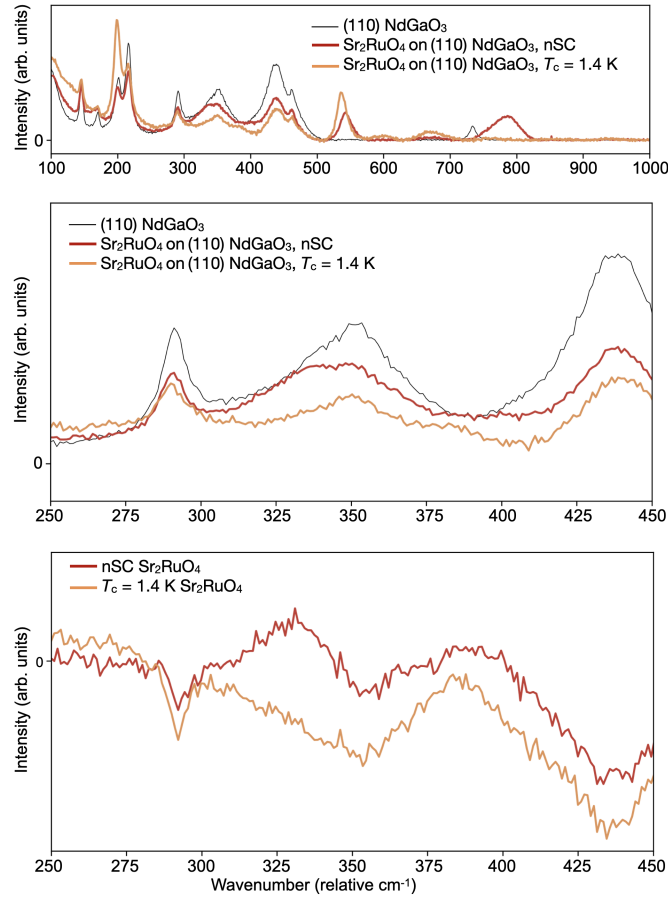


FIG. S9. Confocal Raman spectroscopy measurements of the non-superconducting and $T_c = 1.4$ K Sr_2RuO_4 films. Spectra were acquired in the backscatter geometry using a WITec Alpha300R Confocal Raman microscope equipped with a 532 nm laser source. The propagation of incident light was along the c -axis of the Sr_2RuO_4 films, with polarization along the Sr_2RuO_4 a -axis. The two in-plane crystal axes of (110) NdGaO_3 substrates are distinct and yield different polarized Raman signatures: the measurements presented here are with polarization along the (001) axis of NdGaO_3 . (top) Baseline-corrected confocal Raman spectra of the two films and a bare (110) NdGaO_3 substrate. (middle) Zoomed-in view of the same data above showing the spectral region from ~ 300 cm^{-1} to 400 cm^{-1} identified by Kim, et al.⁵. The substrate signal dominates the measurement. (bottom) The same spectral region with the substrate contribution removed from the measurement of each film. The subtraction is performed by a least squares best fit of the raw data from each film to a constant scale and offset of the substrate reference. The result of this optimization is subtracted from each spectrum to remove the substrate contribution. We note that the NdGaO_3 substrates of our samples are more Raman-active in the spectra range on interest than the LSAT substrates used by Kim, et al., which complicates the substrate correction. Still, the spectral features in the 300 - 400 cm^{-1} range are consistent with the presence of ruthenium vacancies in the non-superconducting film, especially in the peak near 325 cm^{-1} . The strength of this peak is greatly reduced in the superconducting sample, suggesting the second peak near 380 cm^{-1} may be a signature of something other than ruthenium vacancies.

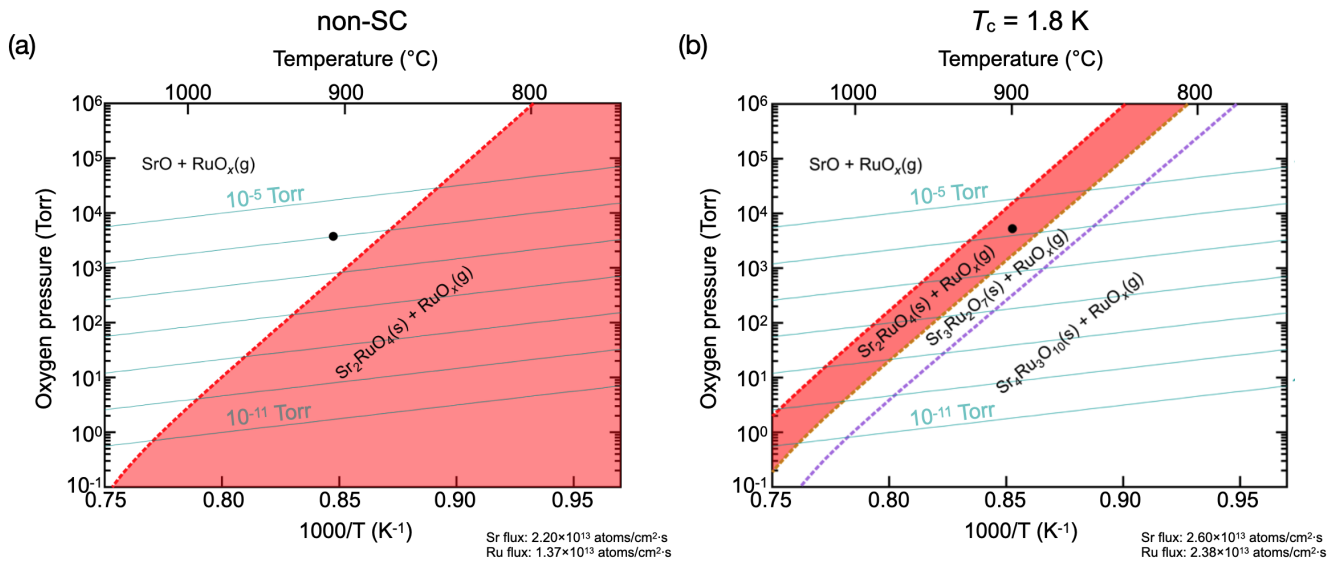


FIG. S10. Calculated thermodynamics of MBE (TOMBE) diagrams⁶ for the (a) non-superconducting and (b) $T_c = 1.8$ K films. The black dot on each diagram indicates the expected phase stability based on calibrated values of strontium and ruthenium fluxes and ozone partial pressure during growth. The cyan lines show the equivalent oxidation potential for ozone partial pressures ranging from 10^{-11} – 10^{-5} Torr. This kind of description is informative for phase-pure films, but does not capture microstructural variation such as the mixed-phase intergrowths observed in the $T_c = 1.4$ K film.

- ¹Hari P. Nair, Jacob P. Ruf, Nathaniel J. Schreiber, Ludi Miao, Morgan L. Grandon, David J. Baek, Berit H. Goodge, Jacob P. C. Ruff, Lena F. Kourkoutis, Kyle M. Shen, and Darrell G. Schlom. Demystifying the growth of superconducting Sr_2RuO_4 thin films. *APL Materials*, 6(10):101108, 2018.
- ²Mark A. Zurbuchen, Yunfa Jia, Stacy Knapp, Altaf H. Carim, Darrell G. Schlom, and X.Q. Pan. Defect generation by preferred nucleation in epitaxial $\text{Sr}_2\text{RuO}_4/\text{LaAlO}_3$. *Applied Physics Letters*, 83(19):3891–3893, 2003.
- ³Jinkwon Kim, Junsik Mun, Carla M. Palomares García, Bongju Kim, Robin S. Perry, Yongcheol Jo, Hyunsik Im, Han Gyeol Lee, Eun Kyo Ko, Seo Hyoung Chang, Suk Bum Chung, Miyoung Kim, Jason W. A. Robinson, Shingo Yonezawa, Yoshiteru Maeno, Lingfei Wang, and Tae Won Noh. Superconducting Sr_2RuO_4 thin films without out-of-phase boundaries by higher-order Ruddlesden–Popper intergrowth. *Nano Letters*, 21(10):4185–4192, 2021.
- ⁴Yawen Fang, Hari P. Nair, Ludi Miao, Berit H. Goodge, Nathaniel J. Schreiber, Jacob P. Ruf, Lena F. Kourkoutis, Kyle M. Shen, Darrell G. Schlom, and B. J. Ramshaw. Quantum oscillations and quasiparticle properties of thin film Sr_2RuO_4 . *Phys. Rev. B*, 104:045152, 2021.
- ⁵Gideok Kim, Y. Eren Suyolcu, J. Herrero-Martin, D. Putzky, H. P. Nair, J. P. Ruf, N. J. Schreiber, C. Dietl, G. Christiani, G. Logvenov, M. Minola, P. A. van Aken, K. M. Shen, D. G. Schlom, and B. Keimer. Electronic and vibrational signatures of ruthenium vacancies in Sr_2RuO_4 thin films. *Physical Review Materials*, 3(9):094802, 2019.
- ⁶Hari P. Nair, Yang Liu, Jacob P. Ruf, Nathaniel J. Schreiber, Shun-Li Shang, David J. Baek, Berit H. Goodge, Lena F. Kourkoutis, Zi-Kui Liu, Kyle M. Shen, and Darrell G. Schlom. Synthesis science of SrRuO_3 and CaRuO_3 epitaxial films with high residual resistivity ratios. *APL Materials*, 6(4):046101, 2018.